

# The dependence of aluminum lattice orientation on semiconductor lattice parameter in planar InAs/Al hybrid heterostructures

Tiantian Wang<sup>a,b,\*</sup>, Candice Thomas<sup>a,b</sup>, Rosa E. Diaz<sup>b</sup>, Sergei Gronin<sup>b,c</sup>, Donata Passarello<sup>d</sup>, Geoffrey C. Gardner<sup>b,c</sup>, Michael A. Capano<sup>b,e</sup>, Michael J. Manfra<sup>a,b,c,e,f</sup>

<sup>a</sup> Department of Physics and Astronomy, Purdue University, West Lafayette, IN 47907, USA

<sup>b</sup> Birck Nanotechnology Center, Purdue University, West Lafayette, IN 47907, USA

<sup>c</sup> Microsoft Quantum Purdue, Purdue University, West Lafayette, IN 47907, USA

<sup>d</sup> Stanford Synchrotron Radiation Laboratory, SLAC National Accelerator Laboratory, Menlo Park, CA 94025, USA

<sup>e</sup> School of Electrical and Computer Engineering, Purdue University, West Lafayette, IN 47907, USA

<sup>f</sup> School of Materials Engineering, Purdue University, West Lafayette, IN 47907, USA

## ARTICLE INFO

Communicated by H. Asahi

### Keywords:

A1. Crystal structure  
A1. Transmission electron microscopy  
A1. X-ray diffraction  
A3. Molecular beam epitaxy  
B2. Semiconducting III–V materials

## ABSTRACT

We present a detailed study of 7-nm thick Al layers epitaxially grown on  $\text{In}_x\text{Al}_{1-x}\text{As}$  or  $\text{Al}_{1-x}\text{Ga}_x\text{Sb}_y\text{As}_{1-y}$  (0 0 1) semiconductors using high-resolution transmission electron microscopy (HRTEM) and synchrotron X-ray diffraction (XRD). These techniques provide high spatial and high reciprocal space resolution information about Al lattice orientations and interfacial structure, highlighting the existence of a strong correlation between the surface lattice parameter of the semiconductor and the normal orientation of the aluminum film. The normal orientation of Al layers is found to be [1 1 1] when the in-plane semiconductor surface lattice parameter,  $a_s$ , is smaller than 5.98 Å, and is [1 1 0] when  $a_s$  is larger than this value. In the transition between these lattice parameters where one orientation is preferred, both orientations may be observed. Concomitant with the change in normal orientation is an inversion in the strain state of the aluminum film. When the normal orientation is [1 1 1], the Al film is compressively strained; while for [1 1 0] normal orientations, the Al in-plane strain is tensile. An energy balance model, accounting for surface, interfacial, side-face, and strain energy, and the registry of (1 1 1) lattice planes across the semiconductor/aluminum interface provide explanations for the observed normal orientation and strain inversion.

## 1. Introduction

The prospect of generating Majorana zero modes (MZM) with specific combinations of semiconducting and superconducting materials is inspiring basic research in hybrid devices. The potential of achieving computational functionality through the control of these quasiparticles is a major scientific objective. Theoretical studies predict the appearance of MZMs at the interface between a s-wave superconductor and a high spin-orbit coupled semiconducting nanowire under the application of an in-plane magnetic field [1–5]. Ideal candidates for the constituent materials supporting the appearance of MZMs are superconducting Al and the low bandgap semiconductors InAs and InSb, both possessing a large g-factor and strong spin-orbit coupling. Experimental signatures consistent with MZMs have been observed in InAs and InSb nanowires coupled to Al or NbTiN superconductors [6–8].

Continued research in the growth and processing of these hybrid

structures has eliminated subgap states and led to the observation of a hard, induced superconducting gap [9–12], enabling the detection of signatures consistent with the presence of MZMs with nearly quantized zero-bias peak of conduction within the gap for both nanowires and planar structures [12–16]. The transition from one to two dimensional structures presents physical differences that are important to consider such as Al domain alignments, strain, and the nature of the transitions in symmetry and lattice parameter.

Disorder in semiconductor-superconductor heterostructures takes on several forms that can potentially affect transport behavior. Aluminum orientational disorder, lack of atomic registry at the interface, grain boundaries, in-plane domain rotations, and stacking disorder can exist in semiconductor-metal heterostructures. Despite extensive research into Al epitaxy on III–V semiconductors, a complete understanding of the relationships between growth parameters, structural characteristics of the semiconductor, and Al nanostructure remain as

\* Corresponding author at: Department of Physics and Astronomy, Purdue University, 1205 West State Street, West Lafayette, IN 47907, USA.

E-mail address: [wang2444@purdue.edu](mailto:wang2444@purdue.edu) (T. Wang).

<https://doi.org/10.1016/j.jcrysgr.2020.125570>

Received 12 February 2020; Received in revised form 19 February 2020; Accepted 20 February 2020

Available online 20 February 2020

0022-0248/ © 2020 Elsevier B.V. All rights reserved.

research objectives. One example is the different Al grain orientations reported in recent literature [9,17,18]. In nanowire heterostructures, Al layers with  $[1\ 1\ 1]$  normal orientation were observed when grown on either the  $(\bar{1}\ 1\ 0\ 0)$  planes of Wurtzite InAs or on the  $(1\ 1\ 1)$ B planes of Zinc Blende InAs [9]. In Ref. 9, the dominant factor controlling Al orientation for thicknesses below 20 nm is the minimization of surface energy. Above this thickness, the strain energy provides a driving force for a transformation in normal orientation from  $[1\ 1\ 1]$  to  $[1\ 1\ 2]$  [9]. Reference 17 shows similar results in 40 nm Al grown on  $[1\ 1\ 1]$ B InAs wires with the notable difference that the Al  $[1\ 1\ 2]$  direction was slightly tilted from the InAs facet normal.

In planar heterostructures, the normal orientation of 5 nm and 10 nm thick Al superconductors, grown on  $\text{In}_{0.81}\text{Ga}_{0.19}\text{As}$  layers atop a semiconducting stack on InP (0 0 1) substrates, was found to be  $[1\ 1\ 1]$  [12]. In a subsequent article by some of the same authors, the Al normal orientation on InAs depended on the composition of the last few monolayers of semiconductor upon which Al metal was deposited [18]. In all cases when Al was grown on a Ga-containing layer,  $[1\ 1\ 1]$  normal orientation was observed. When Al was grown directly on InAs or a thin intermediate AlAs layer, Al exhibited  $[1\ 1\ 0]$  normal orientation. Since Al manifested the same orientation when grown on AlAs or InAs, a dependence of Al normal orientation on the lattice parameter of the top semiconductor layer was not apparent. Instead, interfacial reactivity and interfacial energy minimization were speculated to control Al normal orientation.

This work demonstrates that the lattice parameter of the underlying semiconductor plays an important role in determining Al normal orientation, regardless of the composition of the final few monolayers. We present a detailed study of 7-nm thick Al layers using high-resolution transmission electron microscopy (HRTEM) and synchrotron X-ray diffraction (XRD). These complementary techniques provide high spatial and high reciprocal space resolution information about Al lattice orientations and interfacial structure. To exploit the strengths of these analytical methods, the sample set examined possesses wide variations in surface lattice parameter controlled by varying the composition of  $\text{In}_x\text{Al}_{1-x}\text{As}$  or  $\text{Al}_{1-x}\text{Ga}_x\text{Sb}_y\text{As}_{1-y}$  semiconductor layers. One specific objective is to determine how sensitively the orientation of Al grains depends on the surface lattice parameter of the semiconductor. This investigation offers an innovative perspective on semiconductor-superconductor heterostructures, which can lead to new physical insights about how Al grows on  $[0\ 0\ 1]$  orientated III-V semiconductors.

## 2. Growth of hybrid structures and characterization methods

The molecular beam epitaxy (MBE) of the semiconductor heterostructures took place in a Veeco Gen 930 system. Aluminum was deposited either in the MBE system or in a dedicated metal deposition chamber connected under ultra-high vacuum (UHV). These systems are equipped with traditional in-situ metrology such as RHEED and band edge thermometry. Chambers and materials were prepared with rigorous UHV techniques as described in [19]. Table 1 lists information of the samples characterized. Sample S1–S4 are representative of complete

device structures used in transport experiments and sample S5–S7 are designed to study how Al behaves when deposited onto a surface with different termination (S5) and different lattice parameters (S6 and S7).

For samples S1–S3, InAs quantum wells were grown on semi-insulating InP substrates.  $\text{In}_x\text{Al}_{1-x}\text{As}$  step graded buffer layers (GBL) grown at  $\sim 380^\circ\text{C}$  were used to accommodate the lattice mismatch between the InP substrate and the quantum well region [12,20–22]. For S1 and S2, along the length of the GBL the indium content is graded from 52% to 89%, followed by an inverse grade back to an indium content of 81%. For S3, the indium content is graded from 52% to 84%, followed by an inverse grade back to an indium content of 81%. The GBLs were designed so that the quantum well region,  $\text{In}_{0.75}\text{Ga}_{0.25}\text{As}$  (10 nm)/InAs (7 nm)/ $\text{In}_{0.75}\text{Ga}_{0.25}\text{As}$  (4 nm), is coherently strained. The difference in the design of the GBLs permits a study of how the aluminum layer behaves as a function of semiconductor lattice parameter. These particular semiconductor heterostructures are capped by 2 monolayers of GaAs to serve as an Al etch stop during processing; this layer is identical for S1–S4.

S4 was grown with a heterostructure design allowing further increase of the surface lattice parameter. To do so, the InAs quantum well was grown on an insulating buffer of  $\text{Al}_{0.8}\text{Ga}_{0.2}\text{As}_{0.07}\text{Sb}_{0.93}$  lattice-matched to GaSb (6.096 Å) [23]. The S4 quantum well region,  $\text{In}_{0.9}\text{Al}_{0.1}\text{As}$  (10 nm)/InAs (7 nm)/ $\text{Al}_{0.8}\text{Ga}_{0.2}\text{Sb}$  (7 nm), was designed to be coherently strained to the buffer layer to minimize dislocations. As a result, the surface lattice parameter is close to the value of GaSb. S5 has the same buffer layer design as S4 but with only the InAs (7 nm) layer on top of the buffer layer. Comparison of S4 and S5 shows how the aluminum layer orients itself with different surface atomic species in our experiments.

Samples S6 and S7 were grown to further study the effect on the aluminum layer when growing with other surface lattice parameters. S6 was grown on an InP (0 0 1) substrate with a single  $\text{In}_{0.52}\text{Al}_{0.48}\text{As}$  buffer layer lattice matched to InP (5.869 Å). S7 was grown on an InAs (0 0 1) substrate with an InAs buffer layer so the surface lattice parameter matches InAs (6.059 Å).

After semiconductor growth, samples were cooled down before the aluminum deposition to prevent aluminum from de-wetting [12]. In all cases the substrate was cooled to at least  $-40^\circ\text{C}$ . Two different cooling procedures were used. In the first procedure, the sample remains in the semiconductor growth chamber for 15 h with all heat sources in the chamber idled, this includes turning off the beam flux gauge. The sample radiates heat to a cryopump sitting at approximately  $\sim 40\text{ K}$ . Typical substrate temperature after this procedure was approximately  $-40^\circ\text{C}$  as measured by absorption band edge measurements and a Type C thermocouple. In the second procedure, the sample is transferred to another UHV chamber and contacted by a cooler connected to a source of liquid nitrogen. This allowed faster cooling and somewhat lower temperatures [24]. The temperature estimation for samples cooled in the second deposition chamber is approximately  $-70^\circ\text{C}$  as measured by Type-K thermocouple. We have not observed any appreciable difference between aluminum films deposited in the two chambers. Once the substrate temperature reduces below  $-40^\circ\text{C}$ , de-wetting is eliminated

**Table 1**

Identification and details for samples used in TEM and XRD experiments. Indices to the right of the substrate material are the lattice planes nominally parallel to the surface. In some cases, intermediate layers lie between the substrate and top semiconductor layers. GBL stands for graded buffer layer. For S1–S4, the top layer is the top barrier of an InAs quantum well.

Sample	Substrate	Buffer Layers	Top Layer	GaAs(2ML) Al etch stop
S1	InP (0 0 1)	GBL $\text{In}_{0.52}\text{Al}_{0.48}\text{As}$ to $\text{In}_{0.89}\text{Al}_{0.11}\text{As}$	$\text{In}_{0.75}\text{Ga}_{0.25}\text{As}$	Yes
S2	InP (0 0 1)	GBL $\text{In}_{0.52}\text{Al}_{0.48}\text{As}$ to $\text{In}_{0.89}\text{Al}_{0.11}\text{As}$	$\text{In}_{0.75}\text{Ga}_{0.25}\text{As}$	Yes
S3	InP (0 0 1)	GBL $\text{In}_{0.52}\text{Al}_{0.48}\text{As}$ to $\text{In}_{0.84}\text{Al}_{0.16}\text{As}$	$\text{In}_{0.75}\text{Ga}_{0.25}\text{As}$	Yes
S4	GaSb (0 0 1)	$\text{Al}_{0.8}\text{Ga}_{0.2}\text{As}_{0.07}\text{Sb}_{0.93}$	$\text{In}_{0.9}\text{Al}_{0.1}\text{As}$	Yes
S5	GaSb (0 0 1)	$\text{Al}_{0.8}\text{Ga}_{0.2}\text{As}_{0.07}\text{Sb}_{0.93}$	InAs	No
S6	InP (0 0 1)	N/A	$\text{In}_{0.52}\text{Al}_{0.48}\text{As}$	No
S7	InAs (0 0 1)	N/A	InAs	No

and the orientation of the resulting Al films does not seem to depend on temperature within the range examined. 7 nm thick Al films were evaporated out of a standard MBE effusion cell and deposited at a rate of 0.7 Å/s, measured by in-situ Quartz Crystal Microbalance (QCM) for all samples.

The normal orientations of the aluminum layers of all samples (i.e. the Al lattice direction normal to the surface) are determined by cross-sectional HRTEM imaging using both a Thermo Fisher Tecnai TEM operated at 200 kV and a Thermo Fisher Themis Z Double Corrected TEM operated at 300 kV. TEM samples are cut parallel to (1 1 0) planes of the substrates and are thinned to about 100 nm using both mechanical and ion polishing technique as well as focused ion beam (FIB) lift out techniques. In the microscope, samples are tilted so that a  $\langle 1\ 1\ 0 \rangle$  zone axis is selected.

For sample S3, S5, S6 and S7 (chosen as representatives of different aluminum normal orientations), X-ray experiments were performed using beam line 7.2 at Stanford Synchrotron Radiation Lightsource (SSRL) using monochromatic 13.98 keV or 14.03 keV photons to irradiate samples. Scattered X-rays were collected with a Pilatus 100 k area detector placed 1.014 m from a sample under inspection, corresponding to a horizontal acceptance of 0.33 mrad. Reciprocal space maps (RSM), collected using a Panalytical MRD diffraction system with a Cu X-ray tube, provide lattice parameter data for semiconductor surfaces [25,26]. X-rays passing through the monochromator have a divergence of 28 arcsecs and a wavelength of 1.541 Å.

### 3. Orientation of aluminum grains

Fig. 1(a) shows a HRTEM image of the semiconductor/aluminum interface in S1, and 1(b) the corresponding fast Fourier transformation (FFT) of the aluminum layer showing the reciprocal space of the Al crystal with a  $[1\ \bar{1}\ 0]$  zone axis. The normal orientation of the aluminum layer is found to be  $[1\ 1\ 1]$  for this sample, as well as for samples S3 and S6.

The HRTEM image and corresponding FFT data in Fig. 2 for sample S4, grown on a GaSb substrate, shows the normal orientation for Al is  $[1\ 1\ 0]$ . Same Al orientation is found in samples S5 and S7. Sample S2 was found to have domains with both  $[1\ 1\ 1]$  and  $[1\ 1\ 0]$  normal orientations.

Note that  $[1\ 1\ 0]$  normal orientation of aluminum is found in both S4 and S5, even though they are terminated with different atomic species, GaAs and InAs respectively. It is also notable that S2 contains both  $[1\ 1\ 0]$  and  $[1\ 1\ 1]$  normal orientation in the aluminum layer. It is believed the lattice constant of S2 is at or near the boundary between where  $[1\ 1\ 1]$  and  $[1\ 1\ 0]$  normal orientations in Al layers are favored. Here the nonconformity with the conclusion in reference [18] remains to be understood.

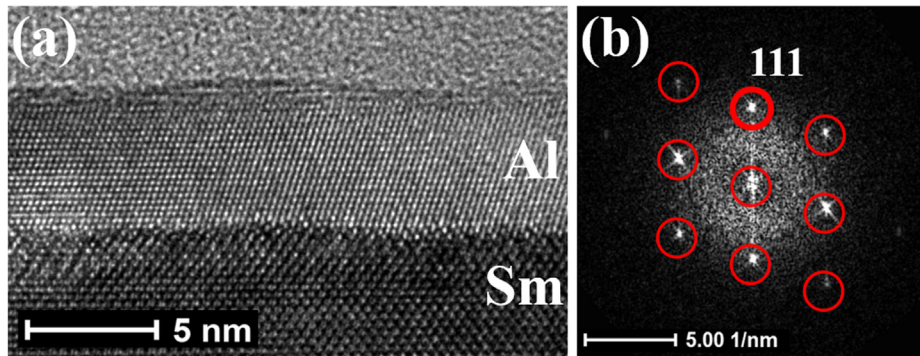


**Fig. 1.** (a) High-resolution TEM image of the aluminum layer (marked “Al”) and the top region of the semiconductor (marked “Sm”) in sample S1. The zone-axis is  $[1\ \bar{1}\ 0]$ . (b) The FFT of the aluminum layer in figure (a) overlapped with a simulated diffraction patterns of Al crystal with zone-axis  $[1\ \bar{1}\ 0]$  marked with red circles. The bold red circle corresponds to the normal orientation of aluminum. (For interpretation of the references to colour in this figure legend, the reader is referred to the web version of this article.)

Table 2 contains a summary of normal orientation for all samples. The table exhibits a clear transition in Al normal orientation from  $[1\ 1\ 0]$  to  $[1\ 1\ 1]$  as the surface lattice parameter of the semiconductor decreases. Sample S2 contains mixed regions with both  $[1\ 1\ 0]$  and  $[1\ 1\ 1]$  Al orientations present. A previous study showed Al taking a  $[1\ 1\ 0]$  normal orientation when deposited onto  $\text{In}_{0.9}\text{Al}_{0.1}\text{Sb}$  (0 0 1) surfaces (lattice parameter 6.42 Å), which supports the transition observed here [24]. To discover what parameter is driving the transformation from one orientation to another, measurements of residual strain in a subset of samples are performed using X-ray diffraction.

In the X-ray diffraction experiments, the Al layer strain in a direction normal to the semiconductor surface is determined using symmetric  $\theta$ - $2\theta$  scans (see Supplementary Information: X-ray configurations). Symmetric scans of the  $(1\ 1\ 1)$  reflection reveal a well-developed peak from S3 as shown in Fig. 3a. The vertical dashed line through the peak at  $q_z = 2.6874\ \text{\AA}^{-1}$  in Fig. 3a represents the position of a strain-free Al  $(1\ 1\ 1)$  peak. A peak shift toward lower  $q_z$  in the figure indicates the presence of a tensile strain normal to the interface. On the other hand, Fig. 3b shows a symmetric scan of the  $(2\ 2\ 0)$  reflection of the Al layer from S5. A compressive normal strain is manifested by a peak shift to higher  $q_z$  relative to the strain-free position at  $q_z = 4.3886\ \text{\AA}^{-1}$ . In summary, Samples S6 which exhibit the same normal orientation  $[1\ 1\ 1]$  as S3, all exhibit normal *tensile* strain. Sample S5 and S7, which exhibit the same normal orientation  $[1\ 1\ 0]$ , all exhibit normal *compressive* strain.

Table 3 summarizes information collected from the XRD sample set. This data includes in-plane lattice parameters, calculated from RSM data, for the topmost semiconductor layer, measured normal strains, and normal orientations. Assuming that Al layers are in a state of biaxial stress and that the in-plane strain components ( $\epsilon_{xx}$ ,  $\epsilon_{yy}$ ) in the Al metal are equivalent, in-plane strains are calculated from normal strain values,  $\epsilon_{zz}$ , using the relation:

$$\epsilon_{xx} = -(C_{11}/2C_{12})\epsilon_{zz} \quad (1)$$

Values for in-plane strains in all samples obtained from Eq. (1) and elastic constants,  $C_{11} = 10.73 \times 10^{10}\ \text{N/m}^2$  and  $C_{12} = 6.08 \times 10^{10}\ \text{N/m}^2$  [27], are listed in Table 3. Noteworthy from Table 3 is the change in strain state between  $[1\ 1\ 1]$  Al (in-plane compression) and  $[1\ 1\ 0]$  Al (in-plane tension) orientations that coincides with the transition of normal orientations.

### 4. Parameters controlling aluminum orientation

In order to explain how different Al orientations may appear, Fig. 4 illustrates an isolated Al grain growing on a semiconductor surface. Four energy density terms describe the thermodynamic state of the grain.  $\gamma_{\text{int}}$  represents the energy density of the interface between the semiconductor and aluminum, and  $\gamma_{\text{surf}}$  represents the energy density of

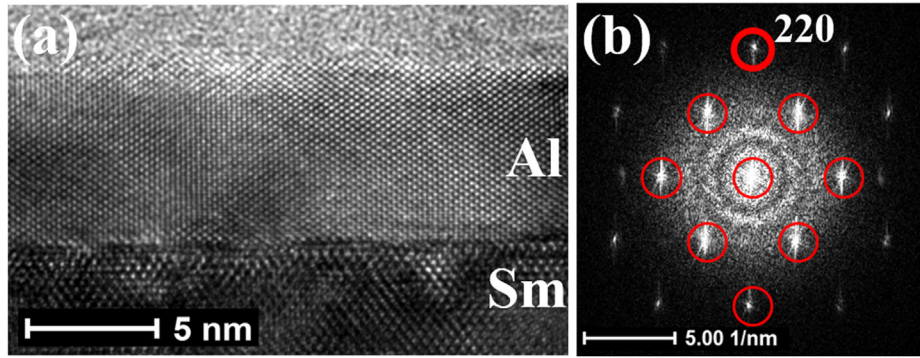


**Fig. 2.** (a) High-resolution TEM image of the aluminum layer (marked “Al”) and the top region of the semiconductor (marked “Sm”) in sample S4. The zone-axis is  $[1\ \bar{1}\ 0]$ . (b) The FFT of the aluminum layer in figure (a) with a simulated diffraction patterns of Al crystal with zone-axis  $[1\ \bar{1}\ 0]$  marked with red circles. The bold red circle corresponds to the normal orientation of aluminum. (For interpretation of the references to colour in this figure legend, the reader is referred to the web version of this article.)

**Table 2**

The relationship between normal orientation of aluminum layers and in-plane lattice parameter on the semiconductor surface. Surface lattice parameters are extracted from measured RSM data (see Supplementary Information to see how surface lattice parameters are measured).

Sample	Surface lattice parameter ( $\text{\AA}$ )	Al normal orientation
S6	$5.87 \pm 0.01$	$[1\ 1\ 1]$
S3	$5.94 \pm 0.01$	$[1\ 1\ 1]$
S1	$5.98 \pm 0.01$	$[1\ 1\ 1]$
S2	$5.98 \pm 0.01$	$[1\ 1\ 0]\&[1\ 1\ 1]$
S7	$6.06 \pm 0.01$	$[1\ 1\ 0]$
S4	$6.10 \pm 0.01$	$[1\ 1\ 0]$
S5	$6.10 \pm 0.01$	$[1\ 1\ 0]$

the top surface of the Al grain. The side facets (sf) of the grain have a generic energy density denoted by  $\gamma_{sf}$  (which becomes the grain boundary energy after coalescence). The energy resulting from each of these terms is area dependent. A fourth energy density,  $\sigma_{str}$ , is from strain within the grain and its energy is volume dependent.

Multiplying each energy density by area or volume and summing terms gives a total energy expression,

$$E_{tot} = E_{surf} + E_{int} + E_{sf} + E_{str}$$

$$= \gamma_{surf} A_{surf} + \gamma_{int} A_{int} + \gamma_{sf} A_{sf} + \sigma_{str} V_{st} \quad (2)$$

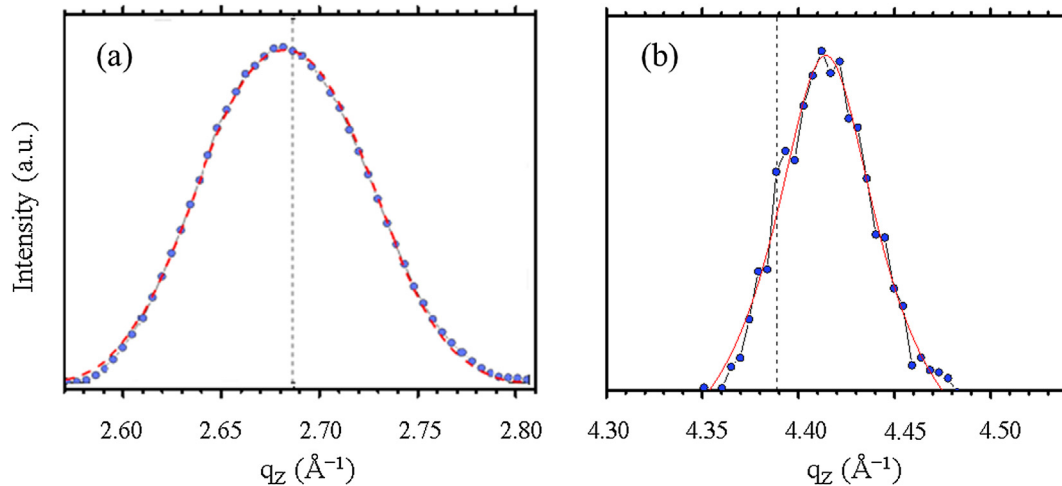


**Fig. 3.**  $\theta$ - $2\theta$  scans of (a) Al  $(1\ 1\ 1)$  reflection from sample S3 and, (b) Al  $(2\ 2\ 0)$  reflection from S5. Dashed vertical lines are peak positions for a strain-free Al  $(1\ 1\ 1)$  peak ( $q_z = 2.687\ \text{\AA}^{-1}$ ) in (a) and strain-free Al  $(2\ 2\ 0)$  peak ( $q_z = 4.388\ \text{\AA}^{-1}$ ) in (b). Red lines are fits to experimental data using a PseudoVoigt function. Shifts toward lower  $q_z$  indicate a normal tensile strain; Shifts toward higher  $q_z$  indicate a normal compressive strain. (For interpretation of the references to colour in this figure legend, the reader is referred to the web version of this article.)

**Table 3**

In-plane lattice parameters extracted from X-ray reciprocal space maps, normal strain in aluminum layer,  $\epsilon_{zz}$ , measured with symmetric X-ray scans, and in-plane Al strain,  $\epsilon_{xx}$ , deduced from normal strains.

Sample	Semiconductor Latt. Param. ( $\text{\AA}$ )	Al normal strain, $\epsilon_{zz}$	Al in-plane strain, $\epsilon_{xx}$	Al normal orientation
S3	$5.95 \pm 0.01$	$0.0029 \pm 0.0003$	$-0.0025$	$[1\ 1\ 1]$
S6	$5.87 \pm 0.01$	$0.0033 \pm 0.0003$	$-0.0029$	$[1\ 1\ 1]$
S5	$6.10 \pm 0.01$	$-0.0015 \pm 0.0003$	$0.0013$	$[1\ 1\ 0]$
S7	$6.06 \pm 0.01$	$-0.0058 \pm 0.0003$	$0.0052$	$[1\ 1\ 0]$

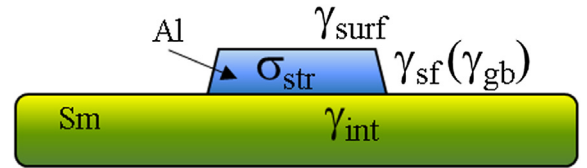


**Fig. 4.** Schematic illustration of a growing Al grain on a semiconductor (Sm) surface. The figure identifies four energy density terms: Surface ( $\gamma_{surf}$ ), interfacial ( $\gamma_{int}$ ), side facet ( $\gamma_{sf}$ ), and strain ( $\sigma_{str}$ ).



Eq. (2) does not imply Al growth is an equilibrium process, but the equation provides a means of incorporating parameters that are lattice-parameter dependent into this analysis. Specifically, strain energy and interfacial energy depend on lattice parameter. Other process parameters, such as growth rate and growth temperature, may cause the boundary between [1 1 1] and [1 1 0] orientated aluminum to shift in lattice parameter by altering kinetic processes, but they themselves do not depend on lattice parameter and are not considered further. The shape of the grain, or nucleus, in Fig. 4 is significant. Measurements of grain size in [1 1 1] orientated Al layers examined in this study (data not presented here) show that Al grain diameters are five times greater than layer thickness. For [1 1 0] layers, the diameter-to-thickness ratio is equal to or greater than ten. A large diameter-to-thickness ratio suggests the true nucleus shape has a flat surface, as depicted in the figure, rather than a lenticular shape. The top surface is assumed to be a high-symmetry, low-energy plane, and this assumption plays a role in the analysis to follow.

The surface energy density term in Eq. (2) is constant. It is widely accepted that in face-centered cubic (FCC) metals, (1 1 1) lattice planes have the lowest surface energy compared to all other planes. For FCC aluminum, reported surface energy density values are 705 ergs/cm<sup>2</sup> for (1 1 1) and 913 ergs/cm<sup>2</sup> for (1 1 0) planes [28]. These values imply that [1 1 1] normal orientation would always be favored over [1 1 0] in the absence of other counterbalancing factors.

One possible counterbalancing quantity is interfacial energy. Fig. 5 presents two cross-sectional images of a semiconductor/Al interface: Fig. 5a for [1 1 0] and Fig. 5b for [1 1 1]. Green lines in the figure identify traces of (1  $\bar{1}$  1) planes in the semiconductor lattice. Red lines coincide with traces of (1  $\bar{1}$  1) planes in aluminum. In Fig. 5a, there is continuity of the {1 1 1} planes across the semiconductor/superconductor interface. This registry at the interface indicates the interfacial energy is low. A different situation appears in Fig. 5b, where there is a mismatch in lattice registry. Some lattice planes in Al (red lines) terminate at the interface and form dislocations, which increase interfacial energy.

Dislocation theory provides an estimate of the difference in interfacial energy between [1 1 0] and [1 1 1] orientated aluminum. If planes terminating at the interface create a dislocation, the core energy of each dislocation is,

$$E_{core} = \frac{Gb^2}{2\pi} \quad (3)$$

where  $G$  is the shear modulus and  $b$  is the magnitude of the Burgers vector [29]. Assuming  $G_{Al} = 25$  GPa [30] and the Burgers vector magnitude is calculated from the Al lattice parameter as  $b_{Al} = 2.86 \times 10^{-8}$  cm, the core energy is about  $3 \times 10^{-5}$  erg/cm. Multiplying this by the lineal density of dislocations along the semiconductor/Al [1 1 1] interface ( $\sim 9$  per 5 nm) yields an interfacial energy density of approximately 580 ergs/cm<sup>2</sup>. This value represents an estimate of how much larger the semiconductor/Al [1 1 1] interfacial energy density is compared to the semiconductor/Al [1 1 0] interface. Interfacial energy density, as developed here from a coherency perspective, shows that [1 1 0] normal orientation is favored over [1 1 1] orientation. When interfacial energy is included in Eq. (2), one can begin to see how the competing influences of interfacial and surface energy may result in either [1 1 1] or [1 1 0] orientation, depending on which energy is dominant. The lower interfacial energy of [1 1 0] Al layers is one counterbalancing quantity that explains the formation of [1 1 0] grains despite its larger surface energy.

Concepts illustrated in Fig. 5 offer a framework for describing how lattice parameter and Al strain influence normal orientation. Considering all data in this study, the normal orientation is [1 1 1] when  $a_s < 5.98$  Å and [1 1 0] when  $a_s > 5.98$  Å. In sample S2, both orientations are present when the lattice parameter is 5.98 Å, which suggests a transition from [1 1 1] to [1 1 0] orientation occurs near this value. A virtual experiment reveals how strain is developed in Al layers as a function of lattice parameter. First, consider the situation shown in Fig. 5a. Suppose the surface lattice parameter of the semiconductor in Fig. 5a is increased above 5.98 Å. Maintaining coherency across the interface requires the (1  $\bar{1}$  1)Al planes to dilate commensurately,

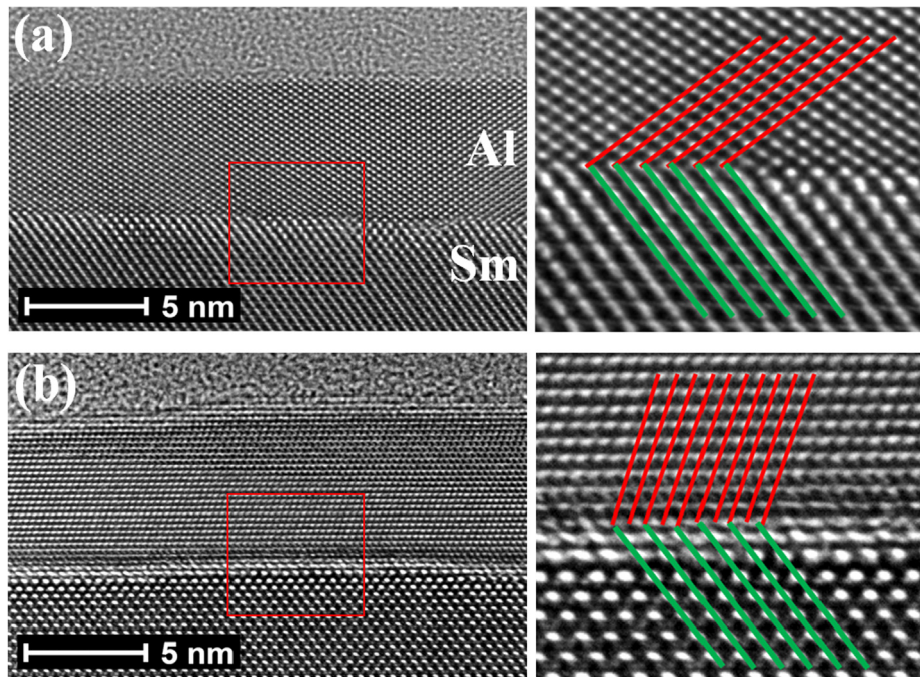


**Fig. 5.** Cross-sectional HRTEM images of semiconductor/Al interfaces having Al normal orientations of (a) [1 1 0] and (b) [1 1 1] both from S2. The interface area in the red boxes are enlarged to show the details of atom registry. Green lines highlight traces of (1  $\bar{1}$  1) planes in the semiconductor. Red lines highlight traces of (1  $\bar{1}$  1) planes in aluminum. In (a), there is one-to-one registry of semiconductor and Al planes. In (b), not all red lines continue into the semiconductor along green traces. This mismatch produces lattice planes that terminate at the interface, increasing the interfacial energy. (For interpretation of the references to colour in this figure legend, the reader is referred to the web version of this article.)

which causes the Al in-plane tensile strain to increase. Although no information about the Al strain state is available for sample S2, the outcome of this virtual experiment, an increased in-plane tension in Al, is consistent with actual X-ray diffraction data in Table 3 for samples S5 and S7 that exhibit [1 1 0] normal orientation.

When the surface lattice-parameter is less than 5.98 Å, Fig. 5a is no longer an accurate representation of Al orientation because [1 1 1] orientation is observed for all lattice parameters below this value. The logic applied to Fig. 5a, however, is equally valid when applied to Fig. 5b. Even though the interface in Fig. 5b is semi-coherent, a decrease in the surface lattice parameter acts to increase the in-plane compressive strain in Al thin layers as the metal attempts to maintain the highest degree of interfacial coherency. This is consistent with actual data in Table 3 which shows in-plane compression for samples S3 and S6 that exhibit [1 1 1] normal orientation. The driving force for maintaining interfacial coherence is the minimization of interfacial energy. Eq. (3) shows there is a large energy cost when interfacial coherence is lost.

A transition in normal orientation occurs at or near a surface lattice parameter 5.98 Å. Near this transition point, it is expected that,

$$(E_{surf} + E_{int} + E_{str} + E_{sf})_{[111]} \approx (E_{surf} + E_{int} + E_{str} + E_{sf})_{[110]} \quad (4)$$

The side facet energy of Al nuclei are unknown, but the assumed shape of a nucleus in Fig. 4 facilitates a simplification of Eq. (4). In the early stages of growth when Al nuclei are two or three monolayers thick,  $E_{sf}$  is small because the total side facet area is small. In nuclei with either [1 1 1] or [1 1 0] normal orientation, the side facets are expected to be aligned along high-symmetry planes because these planes have lower energy than planes of low symmetry. Effectively,  $E_{sf}$  [1 1 1] and  $E_{sf}$  [1 1 0] are equivalent in this situation. Eliminating  $E_{sf}$  terms reduces Eq. (4) to,

$$(E_{int} + E_{str})_{[111]} \approx (E_{surf}[110] - E_{surf}[111]) + (E_{int} + E_{str})_{[110]} \quad (5)$$

Eq. (5) expresses the energy relationship that controls Al normal orientation in the early stages of growth. For the larger lattice parameters examined in this study ( $> 5.98$  Å), Al adatoms can form coherent interfaces with the underlying semiconductor. This causes  $E_{int}$  [1 1 0] to be small enough to compensate for the difference in surface energy between [1 1 0] and [1 1 1] orientations when compared to the semiconductor/Al [1 1 1] interfacial energy. The expected normal orientation is [1 1 0], which matches the observed orientation. When the surface lattice parameter of the semiconductor decreases, Al adatoms can no longer assemble into coherent arrangements as interatomic distances on the surface decrease. This is consistent with the change in the Al in-plane strain state from tension to compression as lattice parameter decreases. In this case, the lower surface energy of [1 1 1] grains enables Al to form with [1 1 1] normal orientation.

Although Eq. (5) was developed using coherency to speak to interfacial energy, the equation is not limited to this perspective. Reference 18 observed normal orientation as a function of composition of the semiconductor surface. A compositional component of the interfacial energy can be included in Eq. (5). One potential method of incorporating surface composition into Eq. (5) is to determine whether surface stoichiometry favors one Al orientation over another based on enthalpies of formation for AlAs, GaAs, and InAs. Such a determination lies outside the scope of this article, which seeks to demonstrate the dependence of Al normal orientation as a function of lattice parameter.

## 5. Summary

In summary, this work demonstrates a strong correlation exists between the surface lattice parameter of the semiconductor and normal orientation of aluminum superconductors. The normal orientation of Al layers is [1 1 1] when the in-plane surface lattice parameter,  $a_s$ , is less than 5.98 Å, and [1 1 0] when  $a_s$  is greater than this value. The Al in-plane strain is compressive when the normal orientation is [1 1 1] and

is tensile when the normal orientation is [1 1 0]. An energy equation and the coherency of the semiconductor/aluminum interface provide explanations for the observed normal orientation and strain inversion.

## CRediT authorship contribution statement

**Tiantian Wang:** Conceptualization, Formal analysis, Investigation, Writing - original draft. **Candice Thomas:** Investigation, Writing - review & editing. **Rosa E. Diaz:** Formal analysis, Investigation, Writing - review & editing. **Sergei Gronin:** Investigation, Writing - review & editing. **Donata Passarello:** Investigation. **Geoffrey C. Gardner:** Investigation, Writing - review & editing. **Michael A. Capano:** Conceptualization, Formal analysis, Investigation, Writing - review & editing. **Michael J. Manfra:** Conceptualization, Writing - review & editing, Supervision, Project administration, Funding acquisition.

## Declaration of Competing Interest

The authors declare that they have no known competing financial interests or personal relationships that could have appeared to influence the work reported in this paper.

## Acknowledgements

This work was supported by Microsoft Quantum. Portions of this research were conducted at the Stanford Synchrotron Radiation Lightsources, a Directorate of SLAC National Accelerator Laboratory and an Office of Science User Facility operated for the U.S. Department of Energy Office of Science by Stanford University. Electron Microscopy sample preparation, data acquisition and analysis in this work used the resources of the Purdue Electron Microscopy at Birck Nanotechnology Center, Purdue University.

## Appendix A. Supplementary material

Supplementary data to this article can be found online at <https://doi.org/10.1016/j.jcrysgro.2020.125570>.

## References

- [1] R.M. Lutchyn, J.D. Sau, S.D. Sarma, Majorana fermions and a topological phase transition in semiconductor-superconductor heterostructures, *Phys. Rev. Lett.* 105 (2010) 077001.
- [2] Y. Oreg, G. Refael, F. von Oppen, Helical liquids and Majorana bound states in quantum wires, *Phys. Rev. Lett.* 105 (2010) 177002.
- [3] J.D. Sau, R.M. Lutchyn, S. Tewari, S. Das Sarma, Generic New Platform for topological quantum computation using semiconductor heterostructures, *Phys. Rev. Lett.* 104 (2010) 040502.
- [4] J. Alicea, Majorana fermions in a tunable semiconductor device, *Phys. Rev. B* 81 (2010) 125318.
- [5] R.M. Lutchyn, E.P.A.M. Bakkers, L.P. Kouwenhoven, P. Krogstrup, C.M. Marcus, Y. Oreg, Majorana zero modes in superconductor-semiconductor heterostructures, *Nat. Rev. Mater.* 3 (2018) 52–68.
- [6] V. Mourik, K. Zuo, S.M. Frolov, S.R. Plissard, E.P.A.M. Bakkers, L.P. Kouwenhoven, Signatures of Majorana Fermions in hybrid superconductor-semiconductor nanowire devices, *Science* 336 (2012) 1003–1007.
- [7] A. Das, Y. Ronen, Y. Most, Y. Oreg, M. Heiblum, H. Shtrikman, Zero-bias peaks and splitting in an Al-InAs nanowire topological superconductor as a signature of Majorana fermions, *Nat. Phys.* 8 (2012) 887–896.
- [8] H.O.H. Churchill, V. Fatemi, K. Grove-Rasmussen, M.T. Deng, P. Caroff, H.Q. Xu, C.M. Marcus, Superconductor-nanowire devices from tunneling to the multichannel regime: Zero-bias oscillations and magnetoconductance crossover, *Phys. Rev. B* 87 (2013) 241401.
- [9] P. Krogstrup, N.L.B. Ziino, W. Chang, S.M. Albrecht, M.H. Madson, E. Johnson, J. Nygard, C.M. Marcus, T.S. Jespersen, Epitaxy of semiconductor-superconductor nanowires, *Nat. Mater.* 14 (2015) 400–406.
- [10] W. Chang, S.M. Albrecht, T.S. Jespersen, F. Kuemmeth, P. Krogstrup, J. Nygard, C.M. Marcus, Hard gap in epitaxial semiconductor-superconductor nanowires, *Nat. Nanotechnol.* 10 (2015) 232–236.
- [11] O. Gul, H. Zhang, F.K. de Vries, J. van Veen, K. Zuo, V. Mourik, S. Conesa-Boj, M.P. Nowak, D.J. van Woerkom, M. Quintero-Perez, M.C. Cassidy, A. Geresdi, S. Koelling, D. Car, S.R. Plissard, E.P.A.M. Bakkers, L.P. Kouwenhoven, Hard superconducting gap in InSb nanowires, *Nano Lett.* 17 (2017) 2690–2696.

- [12] J. Shabani, M. Kjaergaard, H.J. Suominen, Y. Kim, F. Nichele, K. Pakrouski, T. Stankevic, R.M. Lutchyn, P. Krogstrup, R. Feidenhans, S. Kraemer, C. Nayak, M. Troyer, C.M. Marcus, C.J. Palmstrom, Two-dimensional epitaxial superconductor-semiconductor heterostructures: a platform for topological superconducting networks, *Phys. Rev. B* 93 (2016) 155402.
- [13] F. Nichele, A.C.C. Drachmann, A.M. Whiticar, E.C.T. O'Farrell, H.J. Suominen, A. Fornieri, T. Wang, G.C. Gardner, C. Thomas, A.T. Hatke, P. Krogstrup, M.J. Manfra, K. Flensberg, C.M. Marcus, Scaling of Majorana zero-bias conductance peaks, *Phys. Rev. Lett.* 119 (2017) 136803.
- [14] H.J. Suominen, M. Kjaergaard, A.R. Hamilton, J. Shabani, C.J. Palmstrom, C.M. Marcus, F. Nichele, Zero-energy modes from coalescing Andreev states in a two-dimensional semiconductor-superconductor hybrid platform, *Phys. Rev. Lett.* 119 (2017) 176805.
- [15] A. Fornieri, A.M. Whiticar, F. Setiawan, E.P. Marin, A.C.C. Drachmann, A. Keselman, S. Gronin, C. Thomas, T. Wang, R. Kallaher, G.C. Gardner, E. Berg, M.J. Manfra, A. Stern, C.M. Marcus, F. Nichele, Evidence of topological superconductivity in planar Josephson junctions, *Nature* 569 (2019) 89–92.
- [16] A.M. Whiticar, A. Fornieri, E.C.T. O'Farrell, A.C.C. Drachmann, T. Wang, C. Thomas, S. Gronin, R. Kallaher, G.C. Gardner, M.J. Manfra, C.M. Marcus, F. Nichele, Interferometry and coherent single-electron transport through hybrid superconductor-semiconductor Coulomb islands, *arXiv* 1902.07085 (2019).
- [17] N.A. Gusken, T. Rieger, P. Zellekens, B. Bennemann, E. Neumann, M.I. Lespa, T. Schapers, D. Grutzmacher, MBE growth of Al/InAs and Nb/InAs superconducting hybrid nanowire structures, *Nanoscale* 9 (2017) 16735.
- [18] W.L. Sarney, S.P. Svensson, K.S. Wickramasinghe, J. Yuan, J. Shabani, Reactivity studies and structural properties of Al on compound semiconductor surfaces, *J. Vac. Sci. Technol. B* 36 (2018) 062903.
- [19] G.C. Gardner, S. Fallahi, J.D. Watson, M.J. Manfra, Modified MBE Hardware and Techniques and Role of Gallium Purity for Attainment of Two-Dimensional Electron Gas Mobility  $> 35 \times 10^6 \text{ cm}^2/\text{V s}$  in AlGaAs/GaAs Quantum Wells Grown by MBE, *J. Cryst. Growth* 441 (2016) 71–77.
- [20] E.A. Fitzgerald, Dislocations in strained-layer epitaxy: theory, experiment, and applications, *Mat. Sci. Rep.* 7 (1991) 87–142.
- [21] J. Tersoff, Dislocations and strain relief in compositionally graded layers, *App. Phys. Lett.* 62 (1993) 693–695.
- [22] J.E. Ayers, Low-temperature and metamorphic buffer layers, *Handbook of Crystal Growth*, Elsevier B.V., 2015, pp. 1007–1056.
- [23] C. Thomas, A.T. Hatke, A. Tuaz, R. Kallaher, T. Wu, T. Wang, R.E. Diaz, G.C. Gardner, M.A. Capano, M.J. Manfra, High-mobility InAs 2DEGs on GaSb substrates: a platform for mesoscopic quantum transport, *Phys. Rev. Mater.* 2 (2018) 104602.
- [24] C. Thomas, R.E. Diaz, J.H. Dycus, M.E. Salmon, R.E. Daniel, T. Wang, G.C. Gardner, M.J. Manfra, Toward durable Al-InSb hybrid heterostructures via epitaxy of 2ML interfacial InAs screening layers, *Phys. Rev. Mater.* 3 (2019) 124202.
- [25] V.S. Wang, R.J. Matyi, Triple crystal x-ray diffraction analysis of chemical-mechanical polished gallium arsenide, *J. Appl. Phys.* 72 (1992) 5158–5164.
- [26] V.S. Wang, R.J. Matyi, K.J. Nordheden, Triple-crystal x-ray diffraction analysis of reactive ion etched gallium arsenide, *J. Appl. Phys.* 75 (1994) 3835–3841.
- [27] J. Vallin, M. Mongy, K. Salama, O. Beckman, Elastic constants of aluminum, *J. Appl. Phys.* 35 (1964) 1825–1827.
- [28] R.J. Needs, Calculations of the surface stress tensor at aluminum (111) and (110) surfaces, *Phys. Rev. Lett.* 58 (1987) 53–56.
- [29] J.P. Hirth, J. Lothe, *Theory of Dislocations*, Wiley, New York, 1982.
- [30] H.E. Boyer, T.L. Gall, *Metals Handbook*, American Society for Metals, Materials Park, OH, 1985.